Room-temperature observation of near-intrinsic exciton linewidth in monolayer WS$_2$

Jie Fang, Kan Yao, Tianyi Zhang, Mingsong Wang, Taizhi Jiang, Suichu Huang, Brian A. Korgel, Mauricio Terrones, Andrea Alù, Yuebing Zheng*

Jie Fang, Dr. Kan Yao, Dr. Mingsong Wang, Suichu Huang, Prof. Yuebing Zheng

Walker Department of Mechanical Engineering and Texas Materials Institute, The University of Texas at Austin, Austin, TX 78712, USA

E-mail: zheng@austin.utexas.edu

Dr. Tianyi Zhang, Prof. Mauricio Terrones

Department of Materials Science and Engineering, Department of Physics, Department of Chemistry and Center for 2-Dimensional and Layered Materials, The Pennsylvania State University, University Park, PA 16802, USA

Dr. Mingsong Wang, Prof. Andrea Alù

Photonics Initiative, Advanced Science Research Center, City University of New York, New York, NY 10031, USA

Physics Program, Graduate Center, City University of New York; New York, NY 10016, USA

Dr. Taizhi Jiang, Prof. Brian A. Korgel

McKetta Department of Chemical Engineering, The University of Texas at Austin, Austin, TX 78712, USA

Suichu Huang

School of Mechatronics Engineering, Harbin Institute of Technology; Harbin, 150001, China

The homogeneous exciton linewidth, which captures the coherent quantum dynamics of an excitonic state, is a vital parameter in exploring light-matter interactions in two-dimensional transition metal dichalcogenides (TMDs). An efficient control of the exciton linewidth is of great significance, and in particular of its intrinsic linewidth, which determines the minimum timescale for the coherent manipulation of excitons. However, such a control has rarely been achieved in TMDs at room temperature (RT). While the intrinsic A exciton linewidth is down to 7 meV in monolayer WS_2, the reported RT linewidth was typically a few tens of meV due to inevitable homogeneous and inhomogeneous broadening effects. Here, we show that a 7.18 meV near-intrinsic linewidth can be observed at RT when monolayer WS_2 is coupled with a moderate-refractive-index hydrogenated silicon nanosphere in water. By boosting the dynamic competition between exciton and trion decay channels in WS_2 through the nanosphere-supported Mie resonances, we have managed to tune the

coherent linewidth from 35 down to 7.18 meV. Such modulation of exciton linewidth and its associated mechanism are robust even in presence of defects, easing the sample quality requirement and providing new opportunities for TMD-based nanophotonics and optoelectronics.

1. Introduction

Pronounced Coulomb interactions and many-body effects in two-dimensional (2D) transition metal dichalcogenides (TMDs) lead to multiple excitonic states and recombination channels at room temperature (RT), providing a novel platform for exploring light-matter interactions.[1-3] One fundamental property of TMD exciton is its homogeneous exciton linewidth,[4-6] which captures the underlying coherent quantum dynamics and determines the timescale during which excitons can be coherently manipulated.[7-9] However, due to strong multiparticle interactions in TMDs at RT, the coherent exciton linewidth is typically broadened by up to an order of magnitude,[4,5] degrading the quality of excitonic mode and emission.[10-12] Suppressing such homogeneous broadening at RT is thus of great interest, but it has rarely been achieved so far. With the recent achievement of suppressed inhomogeneous contribution,[13,14] the homogeneous broadening has remained as a major fundamental challenge towards the intrinsically narrowest radiation linewidth at RT for TMD emitters. In addition, a controllable narrowing of RT exciton linewidths towards the theoretical limit, i.e., the intrinsic exciton linewidth,[4,7,12] would be of great significance, offering a broad tunability of exciton quantum dynamics for nanophotonic applications. Examples include optical nano-sensors with high spectral resolution and quantum light sources with tunable temporal coherence.

In this work, we couple monolayer WS_2 with single Mie resonators with a moderate refractive index (n) of ~2.1 in water, and directly observe a 7.18 meV near-intrinsic exciton linewidth in the

scattering spectra of the hybrids at RT. The intrinsic exciton linewidth of monolayer WS_2 is calculated to be ~7 meV,[4,5] referred to the minimum coherent manipulation timescale for the bright A exciton (X) located at K (K') points at the Brillouin zone boundaries. In addition, an inherent broadening of ~3 meV always exists even at 0 K[13,14] because of the acoustic Λ phonon emission[4,15] from the energetically lower-lying dark states in tungsten-based TMDs (see **Figure 1A**). Our RT result even surpasses this limit, which can be explained by the dielectric screening in water that lifts the energy level of dark K-Λ state.[16] We show that the linewidth-narrowing mechanism manifests the dynamic competition between exciton and trion decay channels. Specifically, selectively boosting the trion radiative decay via a Mie resonator breaks the charge balancing in inherently n-doped WS_2, and rebuilds the excitonic relaxation processes with suppressed exciton nonradiative decays. Beyond this observation, our work using single hydrogenated silicon (Si) nanospheres represents a practical method to modulate exciton quantum dynamics at the subwavelength scale, successfully tuning the WS_2 exciton linewidth between 35 and 7 meV at RT.

2. Mechanism and design

We first discuss the proposed mechanism for narrowing the exciton linewidth. As shown in Fig. 1A, the K-K exciton quantum dynamics is strongly affected by other dark states through the phonon-induced scattering channels, such as $\gamma_{Xnr}^{K\Lambda}$ and $\gamma_{Xnr}^{KK'}$.[4-6] Accounting the radiative (γ_{Xr}) and nonradiative (γ_{Xnr}^{KK}) decays within the K valley as well, all these recombination pathways determine the homogeneous exciton linewidth γ_X, which is also known as dephasing rate[7-9] in a two-state quantum system (ground $|0\rangle$ and excited exciton $|1\rangle$ states). Consequently, suppression of the homogeneous broadening can be achieved by weakening the contribution from these phonon-induced decay channels at RT. Please note that the influence of spin-forbidden dark states is not included

because the spin flip process is much slower than the exciton-phonon interactions at RT.[6,15] The inhomogeneous broadening due to the local potentials in defected TMD samples does not affect the coherent γ_X,[7,8] and it will be discussed later when we study the incoherent photoluminescence (PL) properties.
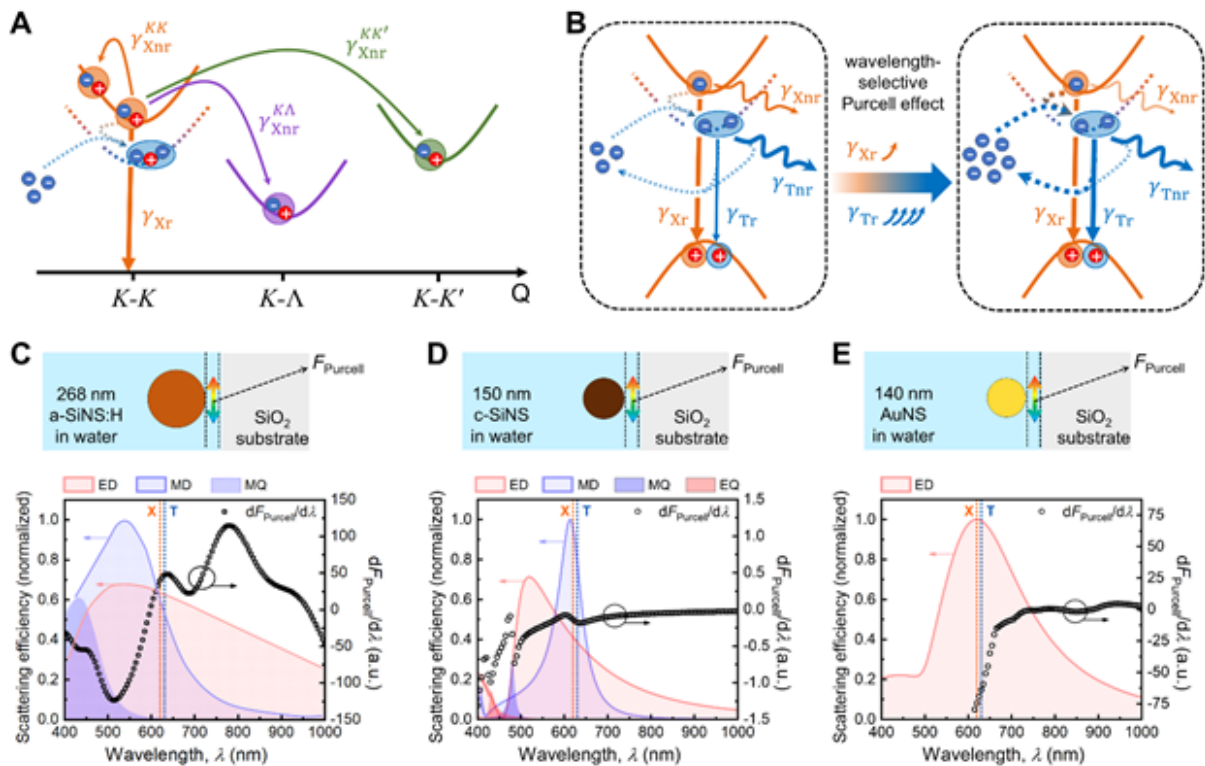

Figure 1. Excitonic relaxation processes in monolayer WS$_2$ and our design of suppressed exciton nonradiative decays based on single spherical resonators. (**A**) Schematic diagram representing the minima of the excitonic center-of-mass motion (Q) dispersion $E(Q)$ of a *K-K* exciton at room temperature. Besides the radiative (γ_{Xr}) and nonradiative (γ_{Xnr}) decays of neutral excitons (X), extra free electrons in the inherently n-doped WS$_2$ lead to the formation of negatively charged trions (T). (**B**) Design of wavelength-selective Purcell effect on exciton (γ_{Xr}) and trion (γ_{Tr}) radiations to suppress

WILEY-VCH

the γ_{Xnr}. Thicker arrows (orange/blue) represent faster decays. Left panel: excitons are radiative (γ_{Xr} dominates) while trions are nonradiative (γ_{Tnr} dominates) without external disturbance. Right panel: originally slow γ_{Tr} shows significant response to the Purcell effect, generating more free electrons to build a new balance in the excitonic system. (**C - E**) Top: A dipole mimicking monolayer WS_2 is positioned between the nanosphere and glass substrate, and the sample is immersed in water. Bottom: (In water) Mode contributions of the spherical resonator and the derivative of Purcell factor ($F_{Purcell}$) versus wavelength for a dipole below the nanosphere: (C) a 268 nm a-SiNS:H, (D) a 150 nm crystalline silicon nanosphere (c-SiNS), and (E) a 140 nm gold nanosphere (AuNS). Exciton (orange) and trion (blue) wavelengths are marked by the dashed lines. The sizes of different spherical resonators are chosen for the best mode wavelength match with the exciton and trion of WS_2. ED, electric dipole; MD, magnetic dipole; EQ, electric quadrupole; MQ, magnetic quadrupole.

Extra free electrons can always be found in WS_2 (see Fig. S1) because of sulfur vacancies,[17] forming negatively charged trions (T) as schematically illustrated in Fig. 1A. Lien *et al.* recently found that the nonradiative decay rate of trion (γ_{Tnr}) is more than two orders of magnitude larger than the radiative one (γ_{Tr}), whereas the exciton decay is dominated by the radiative component ($\gamma_{Xr} > \gamma_{Xnr}$)[18] as shown in the left panel of Fig. 1B. γ_{Xnr} and γ_{Tnr} here represent the total nonradiative contributions. The difference between exciton and trion decay properties can be attributed to a defect-assisted decay and/or a geminate Auger-like process in which the extra electron in trion provides the third particle required for momentum conservation.[18,19] This suggests that the trion total decay rates will be more sensitive to the increase in its radiative decay, e.g., via Purcell effect.[20] Meanwhile, the population densities of exciton (n_X) and trion (n_T) are in dynamic balance as represented by the dashed arrows in Fig. 1B, and follow the law of mass action in steady state as follows,[18,21,22]

$$n_{\text{T}} = K(T_0)n_{\text{X}}n_{\text{e}}, \tag{1}$$

where K is the trion formation coefficient (a constant at a fixed temperature T_0) and n_{e} is the free electron population density. Without electrical gating, the total negative charge concentration $N = n_{\text{T}} + n_{\text{e}}$ is also a constant, and thus Eq. 1 can be written as

$$n_{\text{X}} = (N - n_{\text{e}})/(K(T_0)n_{\text{e}}). \tag{2}$$

According to Eq. 2, if we could selectively enhance the decay of trions, the charge balance will be broken by more free electrons created by the extra trion dissociation, and thus more excitons will be forced to form into trions. Note that since γ_{Tnr} is already fast, we propose to boost γ_{Tr} as shown in the right panel in Fig. 1B. Then, since the trion formation and dissociation times are much shorter than the excitonic lifetimes,[18,22] the overall exciton decays will be significantly suppressed. Further, among all the exciton recombination, considering the originally faster γ_{Xr} than γ_{Xnr}[4,18] and the slightly enhanced γ_{Xr} by Purcell effect (since exciton and trion radiation frequencies are so close), we expect γ_{Xnr} to be suppressed the most. Finally, such a dynamic competition between exciton and trion decays can effectively narrow the γ_{X} down to its near-intrinsic limit at RT, as we experimentally validate in this work. The Purcell effect on γ_{Xr} can also narrow the intrinsic linewidth itself, but the contribution is minor.[4] More discussions can be found in SI Section S7. The outstanding question is how to realize a large contrast in Purcell effects for exciton and trion radiation with only ~30 meV (~10 nm in wavelength) difference.[23] We refer to this requirement as a "wavelength-selective" Purcell effect.

In order to achieve this response, we consider single hydrogenated amorphous silicon nanospheres (a-SiNS:Hs) with ultralow losses at visible frequencies.[24-26] The coupling of WS$_2$ and a-SiNS:Hs not only narrows the γ_{X}, but it also leads to Fano resonances,[27-30] spectrally revealing the

homogeneous property of exciton.[28,31,32] Dielectric nanostructures support both magnetic and electric Mie resonances, while tailoring magnetic optical responses is typically challenging using plasmonic structures.[33-35] Based on the mutual interference of electric (ED) and magnetic dipole resonances (MD), Mie resonators can realize a wide range of near field manipulations within extremely simple geometries,[36] such as a subwavelength nanosphere. In Fig. 1C-E, we calculate the mode contributions of different nanospheres using Mie theory, and simulate the Purcell factor ($F_{Purcell}$) of a dipole, mimicking monolayer WS_2, positioned between the nanospheres and a glass substrate. The derivative of $F_{Purcell}$ versus wavelength is used to better display the wavelength selectivity. The advantage of Mie resonators (Fig. 1C, D) is obvious in comparison with the negative value in the plasmonic one (Fig. 1E). Interestingly, in contrast to a high-refractive-index ($n > 3.0$) dielectric sphere made of pure Si,[29] which supports spectrally separated sharp multipolar modes (Fig. 1D), a moderate-refractive-index ($n = 1.7-3.0$) sphere[36-38] supports broad and overlapped ED and MD (Fig. 1C). This is favorited because the stronger interaction between the two dipole modes can provide larger contrast for wavelength-selective $F_{Purcell}$ as shown in Fig. 1C, and the broader resonances can lead to a more obvious Fano profile. By immersing a 268 nm a-SiNS:H in deionized water ($n = 1.33$), we get an optimal condition, under which both a local maximum of $\mathbf{dF_{Purcell}/d\lambda}$ and ED resonance overlap with WS_2 exciton and trion wavelengths. The analysis in air can be found in Fig. S3. We use water here also because of its large static dielectric constant ($\mathbf{n_{static}} = 80.1$), which decreases the exciton binding energy and thus increases the exciton dipole moment for a stronger coupling with a-SiNS:H.[16,28,31,32,39] In addition, $\mathbf{\gamma_{Xr}}$ increases more than $\mathbf{\gamma_{Tr}}$ under dielectric screening as previously reported,[39] which makes trions more nonradiative compared to excitons. Figure S2 shows this effect in water and it optimizes the narrowing mechanism discussed above. We stress that the total negative charge concentration N remains unchanged and WS_2 is sustainable in our measurements in water as demonstrated in Fig. S2.

WILEY-VCH

3. Experimental results and discussion

Experimentally, we transfer CVD-grown monolayer WS$_2$ on a glass substrate and drop cast a-SiNS:Hs (diameter range: 200-350 nm) on it. The optical signals from a-SiNS:H-WS$_2$ hybrids are collected in a single particle dark-field scattering setup as shown in **Figure 2A**. More details can be found in Methods. WS$_2$ coupled with a 268 nm a-SiNS:H with good sphericity (see the inset in Fig. 2A) is first studied. The measurements in water and air both show a spectrally sharper Fano resonance (Fig. 2B-E) than previously reported results in WS$_2$.[23,28,31,32] As illustrated in Fig. 2B and C, the asymmetric feature at the exciton position is especially prominent and sharp in water, with a quality factor up to 104. We do not observe any coupling features for trions[31,32] owing to their much weaker oscillator strength.[23]

9
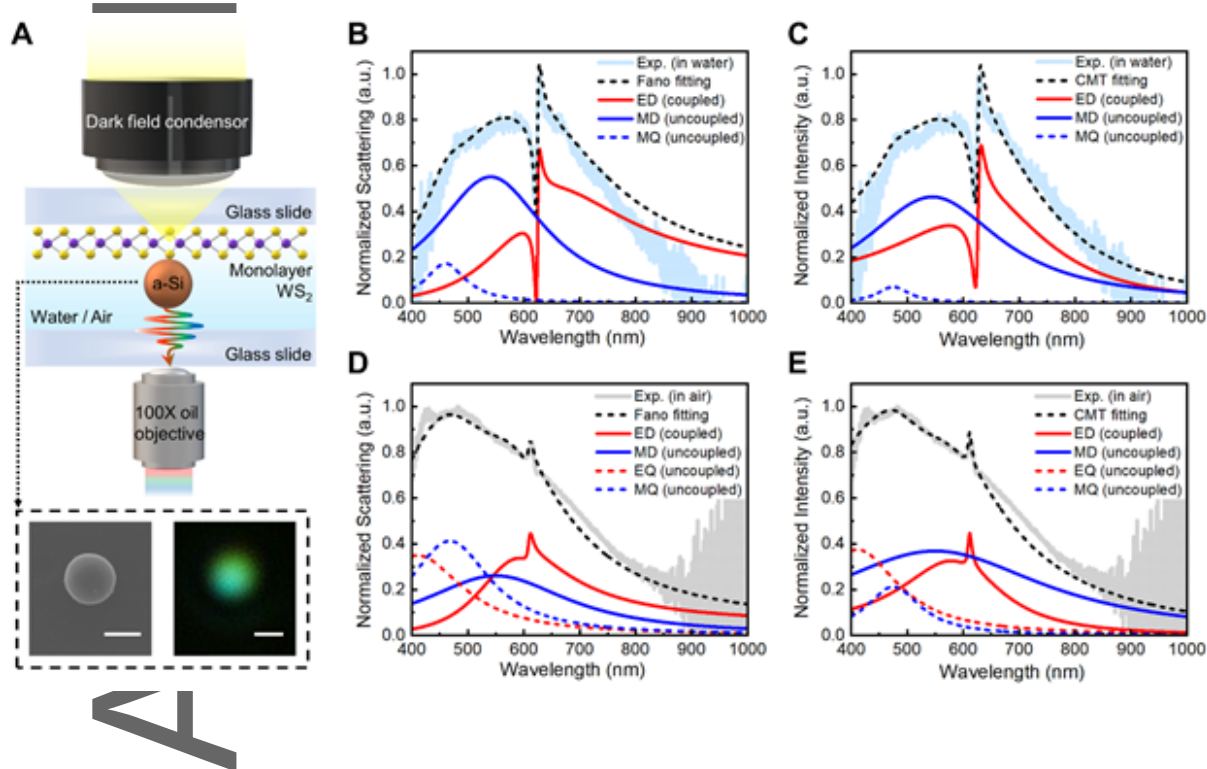
Figure 2. Near-intrinsic exciton linewidth observed in Fano resonances at room temperature.
(**A**) Schematic diagram of the optical setup for single-particle optical scattering measurement. Inset: SEM (left) and dark-field optical (right) images of a 268 nm a-SiNS:H. Scale bar, 200 nm. (**B** and **C**) Scattering spectra of a 268 nm a-SiNS:H coupled with monolayer WS_2 in water and the corresponding (B) Fano and (C) coupled-mode-theory (CMT) fittings. The Lorentz resonance to be included in the coupling with WS_2 exciton (coupled mode) is determined by (Method I) decomposing the Mie resonances (ED is coupled). (**D** and **E**) The same as (B, C), but in air. More details of the fittings can be found in SI Section S11 and Fig. S6. The fitted exciton linewidth and other parameters are concluded in Table 1.

To comprehensively confirm the measured exciton linewidth, we implement both Fano fitting (Fig. 2B, D) and modified coupled mode theory (CMT) fitting (Fig. 2C, E) on the measured spectra. Please see SI Section S8 for more information. In both approaches, a single dipole mode from the Mie resonator is assumed to be interacting/coupled with the highly-confined in-plane WS_2 excitons. In Fig. 2, we define ED as such a coupled Mie mode (Method I) considering its dominant contribution to the in-plane electric field at the monolayer position (See Fig. S4). The fitting results are good in water (Fig. 2B, C) but have distinct deviations in air (Fig. 2D, E) due to the non-ignorable MD contribution as shown in Fig. S5. Therefore, we further utilize the simulated in-plane (coupled) and out-of-plane electric field magnitudes at the monolayer position as Method II to determine a Lorentz resonance to be used for fittings. The details can be found in SI Section S11. Good results are obtained for both water and air cases as illustrated in Fig. S6. The fitted γ_X based on both Methods are listed in Table 1. It is impressive to observe γ_X down to 7.18 meV in water regardless of the fitting method used, reaching the theoretical intrinsic value of ~7 meV.[4,5] As seen in Table 1, the γ_X narrowing effect is a

little weaker in air, and the coupling strength g in water is larger than that in air, both as we expected. But even in water it is still in the weak coupling regime (see more discussions in SI Section S12).

Table 1. Near-intrinsic exciton linewidth (γ_X) obtained from Fano and modified coupled-mode-theory (CMT) fittings**.** The asymmetry parameter q from Fano fitting and the coupling strength g from CMT fitting are also listed.

	γ_X (Fano)	q	γ_X (CMT)	g
In water				
Coupled mode determined by Method I	7.18 meV	-0.77	7.86 meV	157.2 meV
Coupled mode determined by Method II	7.16 meV	-0.79	7.44 meV	148.9 meV
In air				
Coupled mode determined by Method I	16.5 meV	-0.12	17.1 meV	66.2 meV
Coupled mode determined by Method II	14.5 meV	0.11	14.9 meV	49.6 meV

We then perform (in water) control experiments on the a-SiNS:H (resonator) size and inherent WS$_2$ trion (n-doping) concentration, the two important conditions in our design for RT γ_X modulation. Besides the flake 1 that we used for the experimental measurements so far, another flake 2 with less trions is chosen to demonstrate the vital role of trion assistance in suppressing γ_{Xnr}, cf. **Figure. 3A and B**. As shown in Fig. S1, the ratio ($R_{T/X} = \frac{I_{PL\_T}}{I_{PL\_X}}$) of trion PL intensity (I_{PL_T}) to exciton PL intensity (I_{PL_X}) is found to be 2.03 and 0.54 for flakes 1 and 2, respectively. On both flakes, we also

study a few a-SiNS:Hs of different sizes around the optimal size of 268 nm. The SEM images in Fig. 3 reveal the good quality of all the a-SiNS:Hs in study. The measured spectra are normalized and displayed in sequence with respect to the a-SiNS:H size. It is obvious that the Fano line shapes in flake 2 (Fig. 3B) are always broader than those in flake 1 (Fig. 3A) when a-SiNS:Hs of similar sizes are coupled to them, indicating a worse narrowing performance when the trion concentration is low. For both flakes, a consistent variation of the modulated γ_X versus resonator size is observed (see the orange shaded areas): as we deviate from the optimal resonator size, a larger exciton linewidth is coherently contributing to the Fano resonance.
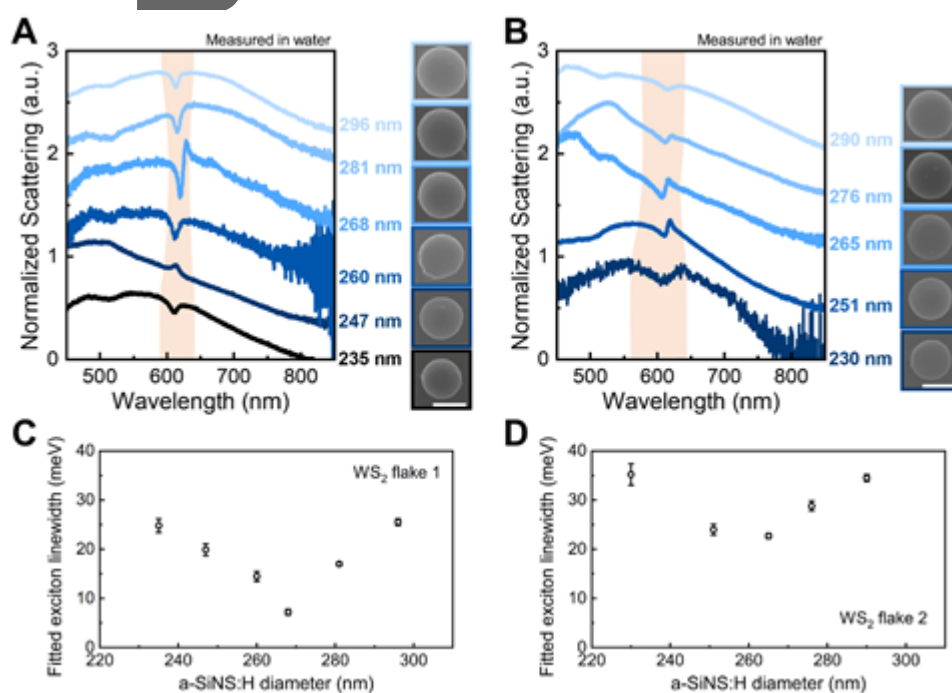

Figure 3. Role of trions and Mie resonators in modulating the coherent exciton linewidth. (**A**) Resonator-size-dependent evolution of the scattering spectra from the hybrid of a-SiNS:H and a WS$_2$ flake with more trions (flake 1, $R_{T/X} = 2.03$). (**B**) The same as (A) but with a WS$_2$ flake with less

trions (flake 2, $R_{T/X} = 0.54$). All the spectra were measured in water. The diameters of the spheres are indicated. The scale bar for all the SEM images is 200 nm. Orange shaded areas roughly guide the eye regarding the change of exciton linewidth. (**C** and **D**) The fitted (see Figs. S7, S8) exciton linewidths of each spectrum in (A) and (B). The exact values of the modulated linewidths are also listed in Table S1.

Fano fittings based on Method I are also implemented on all the spectra in Fig. 3 as displayed in Figs. S7 and S8. The fitted γ_X are drawn in Fig. 3C, D along the axis of a-SiNS:H sizes, quantitatively confirming the predicted variations. The exact retrieved values can be found in Table S1, ranging from 35 to 7 meV. We also simulate the wavelength-selective $F_{Purcell}$ for different resonator sizes (Fig. S9A) and evaluate the resonator-size-dependent values of $dF_{Purcell}/d\lambda$ at the exciton wavelength (Fig. S9B). It is interesting that Fig. 3C and D match well with the reverse of Fig. S9B, validating our design logic from a wavelength-selective Purcell effect towards narrowed γ_X. This can also instruct the on-demand modulation of exciton quantum dynamics at RT based on our platform.
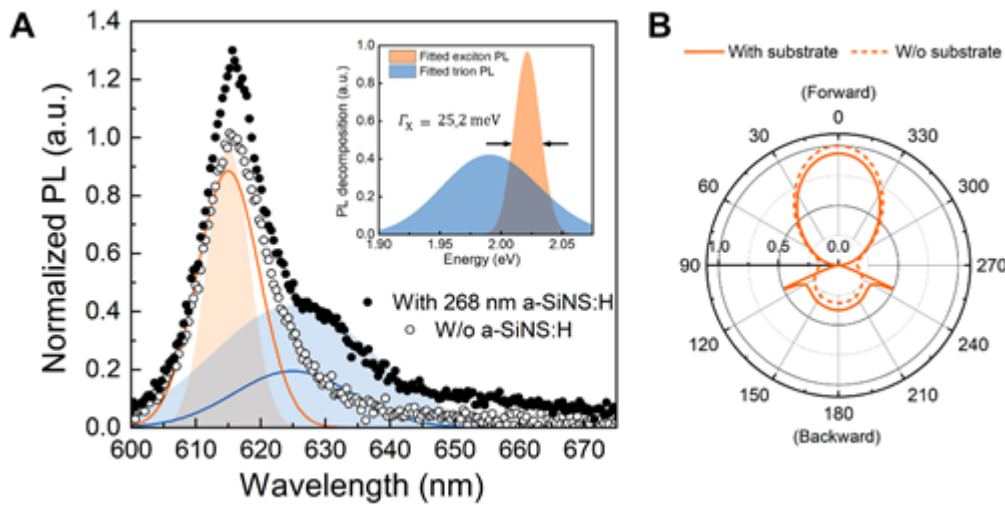
Figure 4. Photoluminescence properties of monolayer WS$_2$ coupled with a-SiNS:H in water. (**A**) Decomposition of measured WS$_2$ photoluminescence (PL) with and without 268 nm a-SiNS:H on it. Orange, exciton; Blue, trion. The shaded peaks (solid lines) are corresponded to the black (white) dots. The directional modulation introduced by a-SiNS:H has been excluded from the raw data for a clearer comparison (black dots).[25] The inset draws the shaded peaks in energy axis and highlights the effective linewidth ($\Gamma_X/2$) of the exciton PL. (**B**) Far-field radiation patterns of a 615 nm dipole (exciton) emission modulated by a 268 nm a-SiNS:H in water when substrate effect is considered (solid line) or neglected (dashed line).

Finally, we study the PL properties of monolayer WS$_2$ coupled with a 268 nm a-SiNS:H in water when a near-intrinsic γ_X is observed. As shown in **Figure 4A**, the enhancement in trion radiation is more significant than that in exciton radiation, in agreement with the wavelength-selective Purcell effect induced by the optimal resonator. Meanwhile, although the PL spectroscopy includes the inhomogeneous contribution,[12] the suppression of the homogeneous broadening can still be observed through the narrowing of the effective exciton linewidth (compare decomposed exciton PL

14

WILEY-VCH

with and without a-SiNS:H). The full width at half maximum of the exciton PL (Γ_X) is found to be ~25.2 meV under a-SiNS:H modulation, as shown in the inset in Fig. 4A. This is smaller than the typical values reported at RT[13,14,29,32] and similar to the results from monolayer WS_2 encapsulated in hexagonal boron nitride[13,14] while no complex fabrication is needed. It is worth noting that our a-SiNS:Hs provide effective directional modulation of exciton emission[25] as shown in Fig. 4B. This effect and the directional modulation of excitation laser[25] have both been excluded from the raw data in Fig. 4A for a clearer comparison. Therefore, we can generate WS_2 emission with both a narrowed spectral linewidth and enhanced directionality at RT.

4. Conclusion

All the monolayer WS_2 flakes we studied are CVD-grown and with considerable defect densities (see the localized states PL in Fig. S1). Impressively, a near-intrinsic γ_X can still be achieved at RT. This offers new opportunities for the broader applications of 2D excitonic systems without stringent requirements of few defects.[40] Sharp optical resonances such as bound states in the continuum[41] at the exciton and trion wavelengths may also lead to the required wavelength-selective Purcell effect. The necessary assistance from trions can be easily generated and tuned electrically in various TMD materials.[18,23] Similar to tunable modulated γ_X via different resonator sizes (Fig. 3), a continuous tunability in the coherent exciton quantum dynamics would also be possible under controllable electrical gating, enabling the developments of tunable 2D sensors, emitters, and electro-optic modulators.

5. Experimental Section

WILEY-VCH

Synthesis of a-SiNS:Hs: A 10 mL titanium batch reactor (High-Pressure Equipment Company (HiP Co.)) is used for the synthesis. First, 21 μL trisilane (Si_3H_8, 100%, Voltaix) and *n*-hexane (anhydrous, 95%, Sigma-Aldrich) are loaded in the reactor in a nitrogen-filled glovebox. The amount of *n*-hexane loaded in the reactor is associated with the reaction pressure inside the reactor during the heating process. The hydrogen concentration in a-SiNS:Hs is determined by the reaction temperature.[26] For example, in this work, we use a-SiNS:Hs with a hydrogen concentration of 40 at.%, which are synthesized at a temperature of 380 °C and a pressure of 34.5 MPa (5000 psi). After adding the reagents, the reactor is sealed by using a wrench inside the glove box. Then a vice is used to tightly seal the reactor after removing it from the glove box. The reactor is heated to the target temperature in a heating block for 10 min to allow the complete decomposition of trisilane. After the reaction, an ice bath is used to cool the reactor to room temperature. Colloidal a-SiNS:Hs are then extracted from the opened reactor. The a-SiNS:Hs are washed by chloroform (99.9%, Sigma-Aldrich) using a centrifuge (at 8000 rpm for 5 min) for three times.

Preparation of Monolayer WS₂: Monolayer WS_2 is synthesized on SiO_2/Si by an atmospheric-pressure chemical vapor deposition (APCVD) method.[25,32] First, powders of WO_3 (5 mg) and NaBr (0.5 mg) are mixed and placed on a piece of SiO_2/Si wafer in an alumina boat. Then another piece of SiO_2/Si (serving as the growth substrate) is placed on the top of the alumina boat facing down and loaded inside a quartz tube. Sulfur powder (400 mg) is loaded in another alumina boat on the upstream. The furnace is ramped up to 825 °C and held for 15 min during synthesis, and sulfur powder is evaporated at 250 °C separately using a heating belt. 100 sccm of argon is used as the carrier gas. As-synthesized monolayer WS_2 is transferred onto glass substrate via a cellulose acetate (CA)-based wet transfer method that we have described previously.[25,32]

Optical Setup and Measurements: An inverted microscope (Nikon TiE) and a spectrograph (Andor

WILEY-VCH

Shamrock 303i-B) with an EMCCD (Andor Newton DU970P) are used for the experiments. A glass coverslip is always applied on the sample to work with an oil immersion objective (Nikon Plan Fluor 100X Oil, NA 0.5). As for the measurement in water, a drop of deionized water is encapsulated between the substrate and coverslip, immersing the WS_2 and a-SiNS:Hs. In the single particle scattering measurement (Fig. 2A), an oil immersion dark-field condenser (Nikon NA 1.20-1.43) is used to focus the white illuminating light (halogen light source, 12 V, 100 W) onto the sample from the top. Forward scattering signal is collected by the 100X oil immersion objective. In the photoluminescence (PL) measurement, a 532 nm laser (Coherent, Genesis MX STM-1 W) is expanded with a 5X beam expander (Thorlabs, GBE05-A) and directed to the microscope. The 100X oil immersion objective is used to focus the laser on the sample and to collect the PL signal. A notch filter (Thorlabs, NF533-17) is used to block the 532 nm laser signal towards the spectrometer. The signal collection window is limited to the single-particle area. The pure WS_2 PL signal is measured five times at different positions surrounding the a-SiNS:H and averaged.

Spectra Fittings: Spectra fittings are performed using MagicPlot software. The Fano and CMT fitting equations are manually written into the software. The error bars in Fig. 3 are the residual standard deviations automatically generated by the software in the fitting process. The software uses iterative Levenberg-Marquardt nonlinear least squares curve fitting algorithm to find the minimum residual sum of squares. The fitting is performed only once for each spectrum and the corresponding residual standard deviation helps describe the root mean square of the error (among all the data points) for the fitted parameters.

Supporting Information

WILEY-VCH

Supporting Information is available from the Wiley Online Library or from the author.

Conflict of Interest

The authors declare no conflicts of interest.

References

[1]   A. Ramasubramaniam, *Phys. Rev. B* **2012**, *86*, 115409.

[2]   A. Chernikov, T. C. Berkelbach, H. M. Hill, A. Rigosi, Y. Li, O. B. Aslan, D. R. Reichman,

M. S. Hybertsen, T. F. Heinz, *Phys. Rev. Lett.* **2014**, *113*, 076802.

[3]   K. F. Mak, C. Lee, J. Hone, J. Shan, T. F. Heinz, *Phys. Rev. Lett.* **2010**, *105*, 136805.

[4]   M. Selig, G. Berghäuser, A. Raja, P. Nagler, C. Schüller, T. F. Heinz, T. Korn, A. Chernikov, E. Malic, A. Knorr, *Nat. Commun.* **2016**, *7*, 13279.

[5]   G. Gupta, K. Majumdar, *Phys. Rev. B* **2019**, *99*, 085412.

[6]   E. Malic, M. Selig, M. Feierabend, S. Brem, D. Christiansen, F. Wendler, A. Knorr, G. Berghäuser, *Phys. Rev. Mater.* **2018**, *2*, 014002.

[7]   G. Moody, C. K. Dass, K. Hao, C.-H. Chen, L.-J. Li, A. Singh, K. Tran, G. Clark, X. Xu, G. Berghäuser, E. Malic, A. Knorr, X. Li, *Nat. Commun.* **2015**, *6*, 8315.

[8]   M. Kira, S. W. Koch, *Prog. Quantum. Electron.* **2006**, *30*, 155.

[9]   M. O. Scully, M. S. Zubairy, *Quantum optics*, Cambridge university press, **1999**.

[10]   P. Dey, J. Paul, Z. Wang, C. E. Stevens, C. Liu, A. H. Romero, J. Shan, D. J. Hilton, D. Karaiskaj, *Phys. Rev. Lett.* **2016**, *116*, 127402.

[11]   S. Koirala, S. Mouri, Y. Miyauchi, K. Matsuda, *Phys. Rev. B* **2016**, *93*, 075411.

[12]   C. Jin, J. Kim, K. Wu, B. Chen, E. S. Barnard, J. Suh, Z. Shi, S. G. Drapcho, J. Wu, P. J. Schuck, S. Tongay, F. Wang, *Adv. Funct. Mater.* **2017**, *27*, 1601741.

[13]   O. A. Ajayi, J. V. Ardelean, G. D. Shepard, J. Wang, A. Antony, T. Taniguchi, K. Watanabe, T. F. Heinz, S. Strauf, X.-Y. Zhu, J. C. Hone, *2D Mater.* **2017**, *4*, 031011.

[14]   F. Cadiz, E. Courtade, C. Robert, G. Wang, Y. Shen, H. Cai, T. Taniguchi, K. Watanabe, H.

WILEY-VCH

Carrere, D. Lagarde, M. Manca, T. Amand, P. Renucci, S. Tongay, X. Marie, B. Urbaszek, *Phys. Rev. X* **2017**, *7*, 021026.

[15]   X.-X. Zhang, Y. You, S. Y. F. Zhao, T. F. Heinz, *Phys. Rev. Lett.* **2015**, *115*, 257403.

[16]   M. Feierabend, G. Berghäuser, A. Knorr, E. Malic, *Nat. Commun.* **2017**, *8*, 14776.

[17]   L. Yang, K. Majumdar, H. Liu, Y. Du, H. Wu, M. Hatzistergos, P. Y. Hung, R. Tieckelmann, W. Tsai, C. Hobbs, P. D. Ye, *Nano Lett.* **2014**, *14*, 6275.

[18].   D.-H. Lien, S. Z. Uddin, M. Yeh, M. Amani, H. Kim, J. W. Ager III, E. Yablonovitch, A. Javey, *Science* **2019**, *364*, 468.

[19]   A. Kurzmann, A. Ludwig, A. D. Wieck, A. Lorke, M. Geller, *Nano Lett.* **2016**, *16*, 3367.

[20]   E. M. Purcell, *Confined Electrons and Photons*, Springer, **1995**, pp. 839-839.

[21]   J. S. Ross, S. Wu, H. Yu, N. J. Ghimire, A. M. Jones, G. Aivazian, J. Yan, D. G. Mandrus, D. Xiao, W. Yao, X. Xu, *Nat. Commun.* **2013**, *4*, 1474.

[22]   J. Siviniant, D. Scalbert, A. Kavokin, D. Coquillat, J. Lascaray, *Phys. Rev. B* **1999**, *59*, 1602.

[23]   B. Munkhbat, D. G. Baranov, A. Bisht, M. A. Hoque, B. Karpiak, S. P. Dash, T. Shegai, *ACS Nano* **2020**, *14*, 1196.

[24]   M. Wang, A. Krasnok, S. Lepeshov, G. Hu, T. Jiang, J. Fang, B. A. Korgel, A. Alù, Y. Zheng, *Nat. Commun.* **2020**, *11*, 5055.

[25]   J. Fang, M. Wang, K. Yao, T. Zhang, A. Krasnok, T. Jiang, J. Choi, E. Kahn, B. A. Korgel, M. Terrones, X. Li, A. Alù, Y. Zheng. *Adv. Mater.* **2021**, *33*, 2007236.

WILEY-VCH

[26]   J. T. Harris, J. L. Hueso, B. A. Korgel, *Chem. Mater.* **2010**, *22*, 6378.

[27]   A. E. Miroshnichenko, S. Flach, Y. S. Kivshar, *Rev. Mod. Phys.* **2010**, *82*, 2257.

[28]   S. Lepeshov, M. Wang, A. Krasnok, O. Kotov, T. Zhang, H. Liu, T. Jiang, B. A. Korgel, M. Terrones, Y. Zheng, A. Alú, *ACS Appl. Mater. Interfaces* **2018**, *10*, 16690.

[29]   H. Wang, J. Wen, W. Wang, N. Xu, P. Liu, J. Yan, H. Chen, S. Deng, *ACS Nano* **2019**, *13*, 1739.

[30]   M. F. Limonov, M. V. Rybin, A. N. Poddubny, Y. S. Kivshar, *Nat. Photonics* **2017**, *11*, 543.

[31]   M. Wang, A. Krasnok, T. Zhang, L. Scarabelli, H. Liu, Z. Wu, L. M. Liz- Marzán, M. Terrones, A. Alù, Y. Zheng, *Adv. Mater.* **2018**, *30*, 1705779.

[32]   M. Wang, Z. Wu, A. Krasnok, T. Zhang, M. Liu, H. Liu, L. Scarabelli, J. Fang, L. M. Liz-Marzán, M. Terrones, A. Alù, Y. Zheng, *Small* **2019**, *15*, 1900982.

[33]   A. I. Kuznetsov, A. E. Miroshnichenko, M. L. Brongersma, Y. S. Kivshar, B. Luk'yanchuk, *Science* **2016**, *354*, 846.

[34]   A. Alù, N. Engheta, *Opt. Express* **2009**, *17*, 5723.

[35]   A. E. Krasnok, A. E. Miroshnichenko, P. A. Belov, Y. S. Kivshar, *Opt. Express* **2012**, *20*, 20599.

[36]   J. A. Schuller, R. Zia, T. Taubner, M. L. Brongersma, *Phys. Rev. Lett.* **2007**, *99*, 107401.

[37]   Z.-J. Yang, R. Jiang, X. Zhuo, Y.-M. Xie, J. Wang, H.-Q. Lin, *Phys. Rep.* **2017**, *701*, 1.

[38]   P. Liu, J. Yan, C. Ma, Z. Lin, G. Yang, *ACS Appl. Mater. Interfaces* **2016**, *8*, 22468.

[39]   Y. Lin, X. Ling, L. Yu, S. Huang, A. L. Hsu, Y.-H. Lee, J. Kong, M. S. Dresselhaus, T. Palacios, *Nano Lett.* **2014**, *14*, 5569.

[40]   P. Dey, J. Paul, Z. Wang, C. E. Stevens, C. Liu, A. H. Romero, J. Shan, D. J. Hilton, D. Karaiskaj, *Phys. Rev. Lett.* **2016**, *116*, 127402.

[41]   E. Melik-Gaykazyan, K. Koshelev, J.-H. Choi, S. S. Kruk, A. Bogdanov, H.-G. Park, Y. Kivshar, *Nano Lett.* **2021**, *21*, 1765.
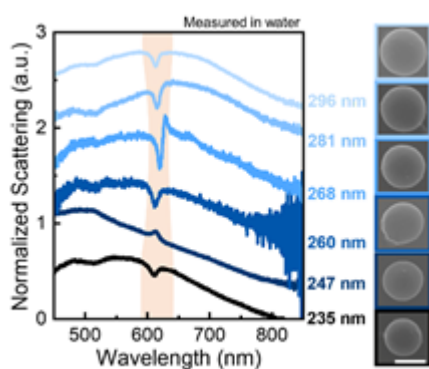
WILEY-VCH

Table of contents

A 7.18 meV near-intrinsic exciton linewidth in monolayer WS_2 is achieved at room temperature by coupling it with a moderate-refractive-index hydrogenated silicon nanosphere in water. The dielectric nanosphere is designed to boost the dynamic competition between WS_2 exciton and trion decay channels and rebuild the excitonic relaxation processes with suppressed exciton nonradiative recombination. A tunable exciton linewidth is also demonstrated.

Jie Fang, Kan Yao, Tianyi Zhang, Mingsong Wang, Taizhi Jiang, Suichu Huang, Brian A. Korgel, Mauricio Terrones, Andrea Alù, Yuebing Zheng*

Room-temperature observation of near-intrinsic exciton linewidth in monolayer WS_2

ToC figure (55 mm broad × 50 mm high)